produced will be randomly distributed inside the crystal. When the faults are able to arrange themselves in a regular fashion, a well ordered polytype is produced; otherwise they are retained as faults in the structure and manifest themselves as streaks between reflections on the X-ray photographs.

In the dendrites grown in an argon atmosphere using analar grade CdI_2, some higher polytypes were observed and the streaking, too, was observed in 9% of cases (Kumar & Trigunayat, 1990). Both higher polytypes and streaking were eliminated when the charge material was well purified by zone refining and the argon atmosphere was replaced by vacuum. Now, when Pb ions are introduced in the CdI_2 structure as impurities, both polytype formation and streaking are again observed. This clearly establishes the role of impurities, including lead, in the formation of polytypes in CdI_2 crystals.

Arcing of the reflections arises from the arrangement of edge dislocations into small-angle tilt boundaries. Like streaking, it has been observed in just 7% of cases in the present work which means that the density of the dislocations produced in the structure was low.

In the earlier work it was found that the melt-grown CdI_2 crystals doped with PbI_2 unusually required long exposure time ($\sim$8–10 h) to produce well exposed X-ray photographs compared with the usual exposure time of nearly 1 h for the undoped CdI_2 crystals (Tyagi & Trigunayat, 1988). It was argued that when the large-sized Pb^{2+} and I^- ions (ionic radii 1·20 and 2·16 Å, respectively) occupy the vacant octahedral voids present in the CdI_2 structure, local displacements are produced which lead to weakening of the X-ray reflections (Vainshtein, Fridkin & Indembom, 1982). However, in the present case of PbI_2-doped dendritic crystals, the time required for producing well exposed X-ray photographs was the same as for the undoped CdI_2 dendritic crystals, viz about 1 h. It follows that no such local displacements are produced

in the present vapour-grown dendritic crystals, the reason for which may be the following. In the melt growth, when the melt solidifies in the growth chamber, the substituted Cd^{2+} ions and the liberated I^- ions cannot escape and are therefore compelled to accommodate themselves at suitable positions in the host structure. This enfored entry of the large I^- ions (ionic radius = 2·16 Å) causes excessive local distortions and hence large local displacements in the structure. No such constraints exist in vapour growth, so the I^- ions are free to escape into the surroundings. They may also combine with the substituted Cd^{2+} ions to form CdI_2 molecules, which may deposit elsewhere in the growth chamber.

References

CHAUDHARY, S. K. & TRIGUNAYAT, G. C. (1982). *J. Cryst. Growth*, **57**, 558–562.
COCHRANE, G. (1967). *Br. J. Appl. Phys.* **18**, 687.
KUMAR, B. & TRIGUNAYAT, G. C. (1990). *Proc. Indian Natl Sci. Acad. Part A.* In the press.
PRAGER, P. R. (1983). In *Crystal Growth and Characterization of Polytypic Structure*, edited by P. KRISHNA, p. 451. Oxford: Pergamon.
SALJE, E., PALOSZ, B. & WRUCK, B. (1987). *J. Phys. C*, **20**, 4077–4096.
TERHELL, J. C. J. M. (1983). In *Crystal Growth and Characterization of Polytypic Structure*, edited by P. KRISHNA, p. 55. Oxford: Pergamon.
TRIGUNAYAT, G. C. (1989). *Phase Transitions*, **16/17**, 509–527.
TRIGUNAYAT, G. C. (1990). *Solid State Ion.* In the press.
TYAGI, U. P. (1988). PhD thesis, Univ. of Delhi, India.
TYAGI, U. P. & TRIGUNAYAT, G. C. (1988). *Acta Cryst.* C44, 1157–1162.
TYAGI, U. P. & TRIGUNAYAT, G. C. (1989). *Phase Transitions*, **16/17**, 537–541.
VAINSHTEIN, B. K., FRIDKIN, V. N. & INDENBOM, L. V. (1982). *Modern Crystallography* II: *Structure of Crystals*. New York: Springer-Verlag.

Thermal Vibrations in Convergent-Beam Electron Diffraction

BY RUSSELL F. LOANE, PEIRONG XU AND JOHN SILCOX

School of Applied and Engineering Physics, Cornell University, Ithaca, New York 14853, *USA*

Abstract

The frozen phonon technique is introduced as a means of including the effects of thermal vibrations in multislice calculations of CBED patterns. This technique produces a thermal diffuse background, Kikuchi bands and a Debye–Waller factor, all of which are neglected in the standard multislice calculation. The frozen phonon calculations match experimental silicon (100) CBED patterns for specimen

thicknesses of up to at least 550 Å. The best-fit silicon r.m.s. vibration amplitude at near room temperature was determined to be 0·085(5) Å. As an independent check of validity, a comparison of calculated CBED, experimental CBED and electron energy loss spectroscopy (EELS) data was also performed. The frozen phonon technique provides an improved theoretical basis for the simulation of CBED and therefore annular dark field scanning transmission electron microscope imaging.

(1) Introduction

Convergent-beam electron diffraction (CBED) is widely used for microcharacterization (Steeds, 1983; Eades, 1988). The most common application is to identify known structures and their orientations, but CBED has also been used to determine accurate unit-cell dimensions (Jones, Rackham & Steeds, 1977), structure symmetries (Goodman, 1975; Tanaka, Saito & Sekii, 1983) and even atomic positions (Vincent, Bird & Steeds, 1984). Strain fields around defects (Fung, 1985; Carpenter & Spence, 1982), specimen thicknesses (Kelly, Jostsons, Blake & Napier, 1975; Kirkland, Loane, Xu & Silcox, 1989), ionicity (Zuo, Spence & O'Keeffe, 1988) and the phase of complex atomic structure factors (Zuo, Spence & Høier, 1989; Bird, James & Preston, 1987) have also been determined.

The sum of the large-angle scattering in the CBED pattern produces the annular dark field (ADF) scanning transmission electron microscope (STEM) image (Langmore, Wall & Isaacson, 1973), which has recently proven capable of resolving atomic structures with Z contrast (Pennycook, 1989; Pennycook, Jesson & Chisholm, 1990) at better than 2 Å resolution (Xu, Kirkland, Silcox & Keyse, 1990; Shin, Kirkland & Silcox, 1989). Three major features of the large-angle scattering are Kikuchi bands (Kikuchi, 1928; Kainuma, 1955; Takagi, 1958), a thermal diffuse scattering (TDS) background (Hall & Hirsch, 1965) and a higher-order Laue zone (HOLZ) ring (Hirsch, Howie, Nicholson, Pashley & Whelan, 1977). Thermal vibrations generate the first two features and reduce the intensity of the third by a Debye–Waller factor (Debye, 1914). Since the intensity in the HOLZ ring may be a significant fraction of the ADF STEM signal (Spence, Zuo & Lynch, 1989), the signal may be sensitive to thermal vibration. There are suggestions that thermal vibrations can change the relative contrast of different elements in the ADF STEM signal (Wang & Cowley, 1989), which differs from the suggestion that the signal is simply related to the atomic cross sections (Pennycook & Jesson, 1990). Accordingly, understanding the effects of thermal vibrations seems necessary for correct interpretation of experimental images. Our previous work on simulating ADF STEM images (Kirkland, Loane & Silcox,

1987; Loane, Kirkland & Silcox, 1988) did not include the effects of thermal vibrations. This paper presents an investigation of the effects of thermal vibrations in CBED as a first step toward exploring the effects in ADF STEM.

Recently, thermal vibrations have been included in multislice calculations by assuming that the vibrations can be averaged to create an effective TDS potential (Wang & Cowley, 1989). In this case, both the elastic and the TDS potentials remain periodic and therefore only scattering at Bragg angles is permitted. Apparently, this technique does not produce a TDS background throughout reciprocal space unless *ad hoc* random phases are introduced.

A beautiful demonstration of the formation of Kikuchi bands by elastic scattering of highly localized inelastic events has been presented (Fan, 1989). In this multislice calculation, the elastic and inelastic wavefunctions are propagated independently through the crystal and then summed incoherently on the detector plane. However, this calculation does not explicitly include the generation of additional inelastic waves throughout the thickness of the crystal.

It is possible to include thermal vibrations in multislice calculations such that TDS, Kikuchi bands and a Debye–Waller factor arise naturally. The basic approximation is that the electron/atom interaction occurs so rapidly that the atom may be considered stationary, *i.e.* the electron sees a snapshot of the atom frozen in mid-vibration. Each atom in the simulated specimen is offset by a small random displacement, typical of its vibration amplitude, and a standard multislice calculation is performed. Each set of random displacements freezes one phonon configuration into the specimen. The calculation is then repeated and averaged (incoherently) over an ensemble of different phonon configurations. This technique is essentially a Monte Carlo integration over phonon configuration space, as discussed below.

(2) Frozen phonon approximation

Atomic vibration periods are on the order of 10^{-13} s (Sinha, 1973; Mitra & Massa, 1982). The large-amplitude acoustic waves, which produce most of the atomic displacement, are many times slower. Classically, a 100 keV electron is a point particle traveling at half the speed of light, $1·5 \times 10^{18}$ Å s^{-1}. If the electron/atom interaction is limited to within a few ångstroms of the atomic nucleus, the interaction time is $\sim 10^{-4}$ vibration periods. In reality, the electron wavefunction is unlocalized along its direction of travel due to a small spread in the time of emission. The length of the wavepacket can be estimated with Heisenberg's uncertainty principle: $\Delta E \, \Delta t \geq h/2$. Assuming a 0·25 eV coherent energy spread for a field emission tip, the emission time is $\sim 2 \times 10^{-15}$ s, the wavepacket length is $\sim 3 \times 10^3$ Å and the interaction

time is $\sim 2 \times 10^{-2}$ vibration periods. Whether the electron is treated classically or quantum mechanically, the electron/atom interaction is much shorter than the atomic vibration period and the vibrating atoms may be considered as frozen in place.

STEM beam currents are on the order of 10^{10} e s^{-1}, so the average time between successive electrons passing through the specimen is about 10^3 atomic vibration periods. This delay is sufficiently large that the atomic displacements seen by successive electrons are essentially uncorrelated. The physical process of accumulating an experimental CBED pattern from millions of electrons, each of which has been scattered by an independent phonon configuration, can be considered as a Monte Carlo integration. This treatment includes Bragg scattering and quasi-elastic phonon scattering but not inelastic scattering.

The electron/specimen interaction can be described by an $N+1$ particle wavefunction, $\Psi(\mathbf{k}, \mathbf{u}_{tot})$, where $\mathbf{k}$ is a three-dimensional electron wavevector and $\mathbf{u}_{tot}$ is a $3N$-dimensional vector denoting the displacement of N atoms from their lattice sites. The joint probability distribution for finding the electron at $\mathbf{k}$ and the atoms at $\mathbf{u}_{tot}$ is then $|\Psi(\mathbf{k}, \mathbf{u}_{tot})|^2$. By definition, this joint probability is the product of the probability of finding the electron at $\mathbf{k}$ given the atoms are at $\mathbf{u}_{tot}$, $P_e(\mathbf{k}|\mathbf{u}_{tot})$ and the probability that the atoms are at $\mathbf{u}_{tot}$, $P_a(\mathbf{u}_{tot})$. Allowing for arbitrary atomic displacements, the probability distribution for the electron (i.e. the electron intensity), I, is given by

$$I(\mathbf{k}) = \int d\mathbf{u}_{tot} P_e(\mathbf{k}|\mathbf{u}_{tot}) P_a(\mathbf{u}_{tot}). \qquad (1)$$

Various phonon dynamics models can be used to determine $P_a(\mathbf{u}_{tot})$. Multislice calculations can be used to determine $P_e(\mathbf{k}|\mathbf{u}_{tot})$. Evaluation of the electron intensity after the specimen yields the CBED pattern. This $3N$-dimensional integral over all possible phonon configurations is far too large to be calculated explicitly but a solution can be determined to any degree of accuracy with Monte Carlo integration.

In principle, each atomic displacement arises from the vector sum of $3N$ normal modes of vibration evaluated at the atom site (Born & von Karman, 1913; Willis & Pryor, 1975). Since the long-wavelength acoustic modes tend to have larger vibration amplitudes, the atomic displacements for neighboring atoms are slightly correlated. To find the correct atomic displacements, it is necessary to determine the amplitude, phase and polarization vector for each of the $3N$ normal modes and then sum them at each of the N lattice sites. In general, the effort required to determine these quantities is tremendous and for the present the simpler Einstein model has been used.

In the Einstein (1907) model, each component of every atomic displacement vector is an independent simple harmonic oscillator (SHO) and all the displacements are uncorrelated with each other. The

energy eigenstate wavefunctions for the SHO, φ_n, as a function of displacement, u, are well known (Sakurai, 1985). By using Planck statistics (Reif, 1965) to determine the occupancy of each of the energy eigenstates, the probability distribution, P_1, for each SHO displacement as a function of temperature, T, is given by

$$P_1(u, T) = \frac{\sum_{n=0}^{\infty} \exp[-(n+\frac{1}{2})\hbar\omega/k_B T]|\varphi_n(u)|^2}{\sum_{n=0}^{\infty} \exp[-(n+\frac{1}{2})\hbar\omega/k_B T]}, \qquad (2)$$

where ω is the oscillator frequency. Substituting in the explicit form for the energy eigenstates and simplifying, one obtains a Gaussian,

$$P_1(u, T) = [(\omega m/\pi\hbar)\tanh(\hbar\omega/2k_B T)]^{1/2}$$
$$\times \exp[-(\omega m/\hbar)u^2\tanh(\hbar\omega/2k_B T)], \qquad (3)$$

where m is the oscillator mass. The Gaussian standard deviation is the r.m.s. atomic displacement, $u_{x\,rms}$, along each component of the 3D displacement vector,

$$u_{x\,rms} = [(\hbar/2\omega m)\coth(\hbar\omega/2k_B T)]^{1/2} \qquad (4)$$

and is often referred to as the vibration amplitude in this paper. The same distribution may be derived from other considerations (Maradudin, Montroll, Weiss & Ipatova, 1971). Experimental r.m.s. atomic displacement values are available in the literature for a limited selection of materials and temperatures (International Tables for X-ray Crystallography, 1974a).

The Einstein model was originally used to describe diamond, a monatomic crystal. In multiatomic crystals, it is not clear how the r.m.s. atomic displacements for the different atoms are related. Since each atom is treated as an independent SHO, the oscillation frequencies in (4) could possibly be different for each site in the crystal. To resolve this issue exactly, one must resort to the more-sophisticated theories where the atomic vibrations are the sum of $3N$ normal modes. Unfortunately, no simple mass dependence can be extracted. The magnitude of the atomic displacement for the different atom types is different for the different normal modes and the relative amplitudes of the normal modes vary with temperature.

The Einstein model approximates the complicated phonon frequency spectrum as a constant for all wavevectors. We apply this same approximation to multiatomic crystals. Since the frequency of oscillation is constant, then by (4) the atomic displacements are proportional to $1/m_i^{1/2}$ where m_i is the atomic mass of the atom at the ith site in the crystal. This approximation is no worse than the original Einstein approximation. A more accurate mass dependence may be found if the relative amplitudes of the different atom types are left as free parameters to be determined from the experimental data. In this paper, the

distribution of the atomic displacements will be assumed to be a Gaussian with a r.m.s. displacement proportional to $1/m_i^{1/2}$.

$$P_1(u_i, T) = \exp\left[-\tfrac{1}{2}(u_i/u_{x\,\mathrm{rms}\,i})^2\right]/(2\pi u_{x\,\mathrm{rms}\,i}^2)^{1/2},$$
$$u_{x\,\mathrm{rms}\,i} = A(T)/m_i^{1/2},$$ (5)

where A is a characteristic vibration amplitude. Except for simple systems (such as silicon) we lack experimental values for A and it must be determined experimentally.

We define a phonon configuration as the entire set of all the random atomic displacements as shown schematically in Fig. 1. Since the atomic displacements are uncorrelated, the probability distribution for phonon configurations is the product of all the probability distributions for all the individual atomic displacements. The probability that the atom positions are $\mathbf{u}_{\mathrm{tot}}$ is then

$$P_a(\mathbf{u}_{\mathrm{tot}})$$
$$= \prod_{i=1}^{N} \prod_{j=x,y,z} \exp\left[-\tfrac{1}{2}(u_{ji}/u_{x\,\mathrm{rms}\,i})^2\right]/(2\pi u_{x\,\mathrm{rms}\,i}^2)^{1/2},$$ (6)

where the j subscript denotes the three components of each atomic displacement vector.

(3) Frozen phonon algorithm

Monte Carlo integration is performed by averaging an ensemble of values of the integrand evaluated at a uniform random sampling of positions in the integration volume. The sampling is increased until the integral converges to the desired level of accuracy. The smoother the integrand is over the integration volume, the faster the convergence.

We must evaluate the integrand of (1), $P_e(\mathbf{k}|\mathbf{u}_{\mathrm{tot}})P_a(\mathbf{u}_{\mathrm{tot}})$, at random positions in the $3N$-dimensional volume of $\mathbf{u}_{\mathrm{tot}}$ space. A uniform sampling of $\mathbf{u}_{\mathrm{tot}}$ space would produce many positions far out in the tails of the Gaussian, $P_a(\mathbf{u}_{\mathrm{tot}})$, which make small contributions to the integral. A more-efficient calculation is achieved by using $P_a(\mathbf{u}_{\mathrm{tot}})$ as the probability distribution for the sampling positions in $\mathbf{u}_{\mathrm{tot}}$
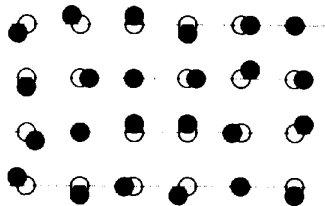

Fig. 1. Schematic diagram of one frozen phonon configuration. All the atoms (solid circles) are frozen in mid-vibration at small displacements from their atomic sites (open circles). Other phonon configurations would have the atoms frozen at different random displacements.

space and then evaluating only $P_e(\mathbf{k}|\mathbf{u}_{\mathrm{tot}})$ at those positions. In this case, each position contributes equally to the integral; there are just fewer positions located out in the tails of the Gaussian. Changing the distribution of sampling positions is a standard Monte Carlo procedure (Press, Flannery, Teukolsky & Vetterling, 1986) and corresponds to a change of variables in the integral.

The frozen phonon algorithm is as follows: First, all the atoms in the simulated specimen are offset by random displacements as determined by the probability distribution, $P_a(\mathbf{u}_{\mathrm{tot}})$, to create one phonon configuration. Second, a multislice calculation is performed to determine the CBED pattern, $P_e(\mathbf{k}|\mathbf{u}_{\mathrm{tot}})$, for that phonon configuration. These two steps are repeated and the CBED patterns are averaged over an ensemble of configurations until the desired level of accuracy is reached. A natural consequence of explicitly calculating the scattering from each phonon configuration is the inclusion of multiple elastic and TDS scattering to all orders.

A CBED multislice calculation begins with the generation of an incident wavefunction on the entrance surface of the specimen. In this paper the Bragg discs do not overlap and the incident probe width is broad compared to the interatomic spacings. Therefore, the incident-probe position is irrelevant and will be assumed to lie at the origin. Then the probe is evolved through the specimen with the multislice algorithm which involves repeated scattering from a slice of atoms and propagation to the next slice. The essential relationship (Loane, Kirkland & Silcox, 1988) is given by

$$\psi_{i+1}(\mathbf{x}) = t_i(\mathbf{x})[\psi_i(\mathbf{x}) \otimes p(\mathbf{x})],$$ (7)

where ψ_i is the electron wavefunction before the ith slice, t_i is the ith slice transmission function and p is the propagator function. This multislice algorithm has been described in detail elsewhere (Cowley & Moodie, 1957; Goodman & Moodie, 1974; Ishizuka & Uyeda, 1977; Kirkland, Loane & Silcox, 1987; Loane, Kirkland & Silcox, 1988). The intensity of the outgoing wavefunction (as a function of wavevector) from the final slice is the CBED pattern. The CBED multislice calculation is valid for relatively thick specimens and includes the effects of dynamical diffraction, channeling, scattering to fractional Bragg angles, HOLZ scattering and arbitrary specimen structure, provided that sufficient computer resources are available.

The simulated specimen is composed of a stack of slice transmission functions (slices), each of which represents a single layer of atoms. At first glance, the frozen phonon technique appears to require the calculation of a multitude of different slices to describe all the atomic displacements in the ensemble of specimen phonon configurations. However, a shortcut is possible within the Einstein approximation. Since the

random atomic displacements in one unit cell do not depend on the random displacements in any other unit cell, rearranging the unit cells produces a different but equally valid phonon configuration. Randomly reordering unit cells enables a few slices to appear as many different phonon configurations. In reality, normal modes of vibration extend throughout the entire specimen and unit cells cannot be reordered without destroying the correlations caused by long-wavelength phonons. Within the Einstein approximation the atomic vibrations are uncorrelated, the shortcut is valid and any real correlations are neglected.

In CBED multislice calculations, the slice transmission functions must contain many unit cells to determine the scattering at fractional Bragg angles. If the slice is shifted horizontally by an integral number of unit cells, the electron wavefunction encounters a different set of random atomic displacements and the same slice appears to be a new slice with a different phonon configuration. Different random stacking sequences and random horizontal shifts produce different phonon configurations. The number of slices required to represent adequately the entire ensemble of phonon configurations increases as the number of unit cells per slice decreases. The validity of this shortcut is easily tested by increasing the number of slices used until the results converge to the desired level of accuracy.

Given a random number generator (Press, Flannery, Teukolsky & Vetterling, 1986) the shortcut modification to the multislice algorithm of (7) is trivial.

$$\psi_{i+1}(\mathbf{x}) = t_{ij}(\mathbf{x} - n\mathbf{a} - m\mathbf{b})[\psi_i(\mathbf{x}) \otimes p(\mathbf{x})], \quad (8)$$

where j, n and m are random integers and $\mathbf{a}$ and $\mathbf{b}$ are crystal lattice vectors perpendicular to the beam. The j random number selects a slice from a set of many ith slices which differ only by their random atomic displacements. Then the n and m random numbers determine the number of unit cells the slice is shifted horizontally.

CBED patterns and the frozen phonon approximation are described in terms of the electron wavevector, $\mathbf{k}$. An equivalent form of the frozen phonon algorithm can be written in terms of $\mathbf{k}$ by Fourier transforming (8).

$$\Psi_{i+1}(\mathbf{k}) = [T_{ij}(\mathbf{k}) \exp[-2\pi i \mathbf{k} \cdot (n\mathbf{a} + m\mathbf{b})]$$

$$\otimes [\Psi_i(\mathbf{k})P(\mathbf{k})], \quad (9)$$

where the upper-case functions in (9) represent the Fourier transforms of the corresponding lower-case functions in (8). Thus, the horizontal shift of the slice transmission functions can be accomplished in reciprocal space by multiplication with a phase factor which is easier to implement numerically.

No modification of the slice transmission function generation is necessary but the atom position inputs must be changed to include the random atomic vibration displacements. Given a characteristic vibration amplitude, (5) dictates the standard deviation of the Gaussian displacement distribution for each atom in the slice. A Gaussian random number (Press, Flannery, Teukolsky & Vetterling, 1986) is added to each component of every atomic position and then the slice transmission function is calculated normally (Loane, Kirkland & Silcox, 1988). We still calculate our slices from X-ray scattering factors (*International Tables for X-ray Crystallography*, 1974b) instead of electron scattering factors (Doyle & Turner, 1967) because the Mott (1930) formula ensures the correct asymptotic form for high-angle scattering.

Within the Einstein approximation, the atomic displacements can be broken up into independent components and considered individually. For 100 keV electrons, the scattering is insensitive to small atomic displacements along the optical axis (z axis). The z component of thermal vibration gives rise to TDS and a Debye–Waller factor along $\mathbf{k}_z$, just as the x (and y) components do along $\mathbf{k}_x$ (and $\mathbf{k}_y$). As shown below, the effects of vibration increase with $\mathbf{k}_x$ and are extremely small for $\mathbf{k}_x < 0.5$ Å^{-1}. Since the scattering vector has a small $\mathbf{k}_z$ component, even for the HOLZ scattering ($\mathbf{k}_z < 0.2$ Å^{-1}), the z displacement component has little effect. Only the projection of the atomic potentials along the z axis is used to create multislice slice transmission functions. The z displacement component is lost in this projection. The slice transmission functions and therefore the entire calculation only contain atomic displacements along x and y.

(4) Calculation parameters and sampling

The primary concern when performing a frozen phonon calculation is whether enough phonon configurations have been averaged to represent the ensemble adequately. Fig. 2 shows a series of CBED patterns calculated with increasing number of phonon configurations. If too few configurations are used, the intensity distribution of the CBED pattern contains too much random noise to provide much meaningful information. Good results can be achieved with just 16 phonon configurations.

In some cases, the symmetry in the CBED pattern can be used to reduce the random variation. For example, the CBED patterns in Fig. 2 could be (but were not) added to their four (110) plane mirror images, doubling their signal-to-noise ratios. Such an approach has the danger of forcing an incorrect symmetry on the pattern.

All CBED patterns displayed in this paper have been logarithmically transformed in order to bring out their low-intensity features. The intensity

Table 1. *The resolution and extent in real and reciprocal space of the calculation are determined by the number of pixels and the extent of the real-space arrays*

The maximum included scattering angle is the radius of the usable portion of the reciprocal-space array after band width limiting.

N_x, N_y	Array dimensions	512 pixels
n_x, n_y	Number of unit cells	6 cells
X, Y	Real-space array extent	35·2 Å
X/N_x, Y/N_y	Real-space array resolution	0·069 Å
$\lambda N_x/X$, $\lambda N_y/Y$	Reciprocal-space array extent	538 mrad
λ/X, λ/Y	Reciprocal-space array resolution	1·05 mrad
$\lambda/3$ min $(N_x/X, N_y/Y)$	Maximum included scattering angle	179 mrad

displayed, I', is related to the original intensity, I, by

$$I'(\mathbf{k}) = \ln\left[1 + CI(\mathbf{k})/I_{max}\right], \qquad (10)$$

where $\mathbf{k}$ represents the scattering angle and $C = 3000$ was arbitrarily chosen as aesthetically pleasing. The calculated CBED patterns have also been clipped so that a close up of the most interesting portion of the pattern is displayed.

A related sampling issue is whether the number of different slice transmission functions is large enough so that the shortcut (described above) is valid. To test the shortcut validity, identical calculations of indium phosphide were performed with sets of 1, 2 and 4 slices which differed only in their random atomic displacements. To the level of accuracy provided by 64 phonon configuration ensembles, there is no difference between using one slice transmission function and four. This result is not surprising since each slice contains 6 × 6 zinc-blende unit cells for a total of 72 equivalent sites per slice, which should be enough instances to represent a Gaussian distribution of atomic displacements. The effort to calculate four slices is relatively small and as long as they all fit in computer memory at once there is no additional cost in using four. Throughout this paper, we have used four slices (288 equivalent sites) in a random stacking sequence with random horizontal shifts to produce all the phonon configurations in the ensemble.

As in any multislice calculation, the slice dimensions in pixels and ångströms must be chosen carefully. These choices dictate the extent (array size) and resolution (pixel size) of the calculation in position (real space) and scattering angle (reciprocal space) as summarized by the relations in Table 1. The reciprocal-space array must be densely sampled to represent adequately the fine structure of the CBED pattern and large enough to include the TDS and HOLZ ring after bandwidth limiting (Loane, Kirkland & Silcox, 1988). These conflicting requirements result in a large number of pixels and therefore long calculation times. A single 512 × 512 pixel slice takes ~2 s to calculate on a Convex 210 minisupercomputer. Therefore, a 400 slice standard multislice calcu-

lation takes ~13 min to calculate and a 16 configuration frozen phonon calculation takes ~3·5 h.

We have used a variety of III/V compounds* and silicon in the (100) orientation in our calculations. These specimens all have the same zinc-blende structure and nearly identical lattice parameters, so one sampling test should apply to all. To test whether the slice dimensions were sufficient, 6 × 6 unit-cell calculations at 512 × 512 pixels were compared to 9 × 9 unit-cell calculations at 1024 × 1024 pixels which have larger extent and resolution in both real and reciprocal space. Calculations were performed with 587 Å (400 slices) of untilted indium phosphide (100). The indium r.m.s. atomic displacement was 0·10 Å and the phosphorus displacement was 0·192 Å. The incident probe modeled the Cornell VG-HB501 STEM (100 keV) with the low-resolution pole piece ($C_s = 3·3$ mm) at Scherzer focus ($\alpha_{ap} = 8·18$ mrad, $\Delta f = 1105$ Å). To the level of accuracy provided by 64 phonon configurations in the ensemble, there was no difference between the two calculations for scattering angles up to 160 mrad. Scattering in the range of 160 mrad to the bandwidth limit at 179 mrad was underestimated by the smaller calculation.

Finally, the slice thickness must be sufficiently thin to be accurately treated as a phase object and to represent correctly the three-dimensional structure information in the HOLZ rings. All calculations presented in this paper were performed with four slices per zinc-blende unit cell. Each of these extremely thin slices, <1·5 Å, contains only one plane of atoms.

(5) Calculation results

Calculations were performed to explore the effects of varying the thermal vibration amplitude. We expect the intensity of the Bragg scattering to decrease by a Debye–Waller factor as the amount of thermal vibration is increased. Calculated CBED patterns in Fig. 3 show that the intensity lost from the Bragg scattering creates a TDS background. Scattered intensities as a function of scattering angle for the same thicknesses are plotted in Fig. 4. These curves are the result of azimuthal integrations around circles of constant $|\mathbf{k}|$ in the CBED patterns of Fig. 3 and provide a more quantitative view of the same data.

Without vibrations, there is essentially no scattering between the low-order Bragg beams and the HOLZ ring. As the amount of vibration is increased, intensity is shifted out of both the HOLZ ring and the low-order Bragg beams and into the TDS background. The r.m.s. atomic displacement for silicon is about 0·07 Å at room temperature (*International Tables for X-ray Crystallography*, 1974a). At large vibration amplitudes, 0·15 Å, the HOLZ ring completely disappears. As the amount of vibration increases, the low-order

---

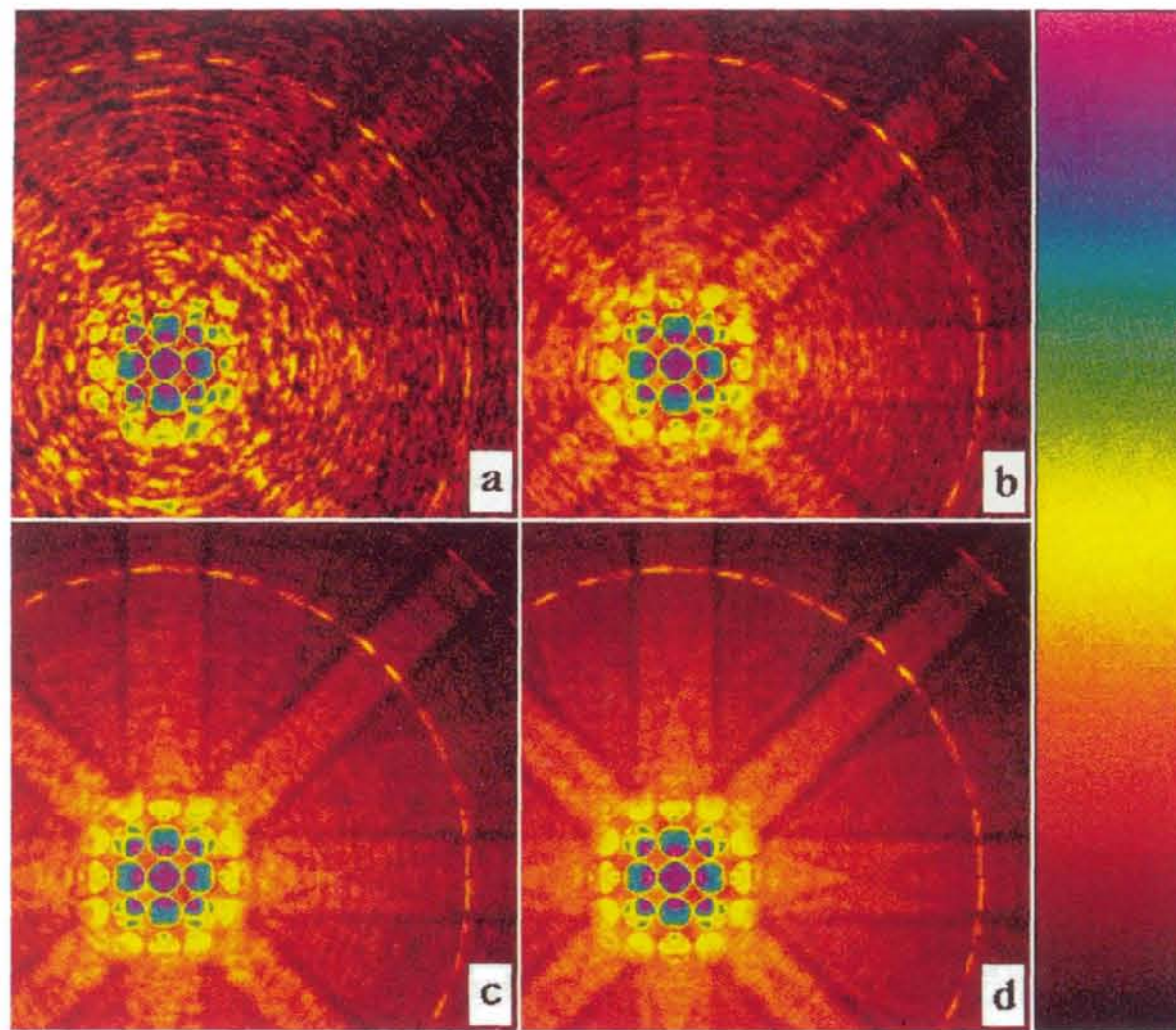* 3/5 compounds in IUPAC (1990) nomenclature.

Fig. 2. Phonon configuration series of CBED calculations performed for a 273 Å (200 slices) thick specimen of untilted gallium phosphide (100). The number of phonon configurations averaged were (*a*) 1, (*b*) 4, (*c*) 16 and (*d*) 64. The slice dimensions were 512×512 pixels and 6×6 unit cells, which is $32 \cdot 7 \times 32 \cdot 7$ Å. The gallium r.m.s. atomic displacement was $0 \cdot 08$ Å and the phosphorus displacement was $0 \cdot 12$ Å. The incident probe modeled the Cornell VG-HB501 STEM (100 keV) with the low-resolution pole piece ($C_s = 3 \cdot 3$ mm) and a small objective aperture ($\alpha_{ap} = 6 \cdot 0$ mrad) near optimum focus ($\Delta f = 600$ Å).
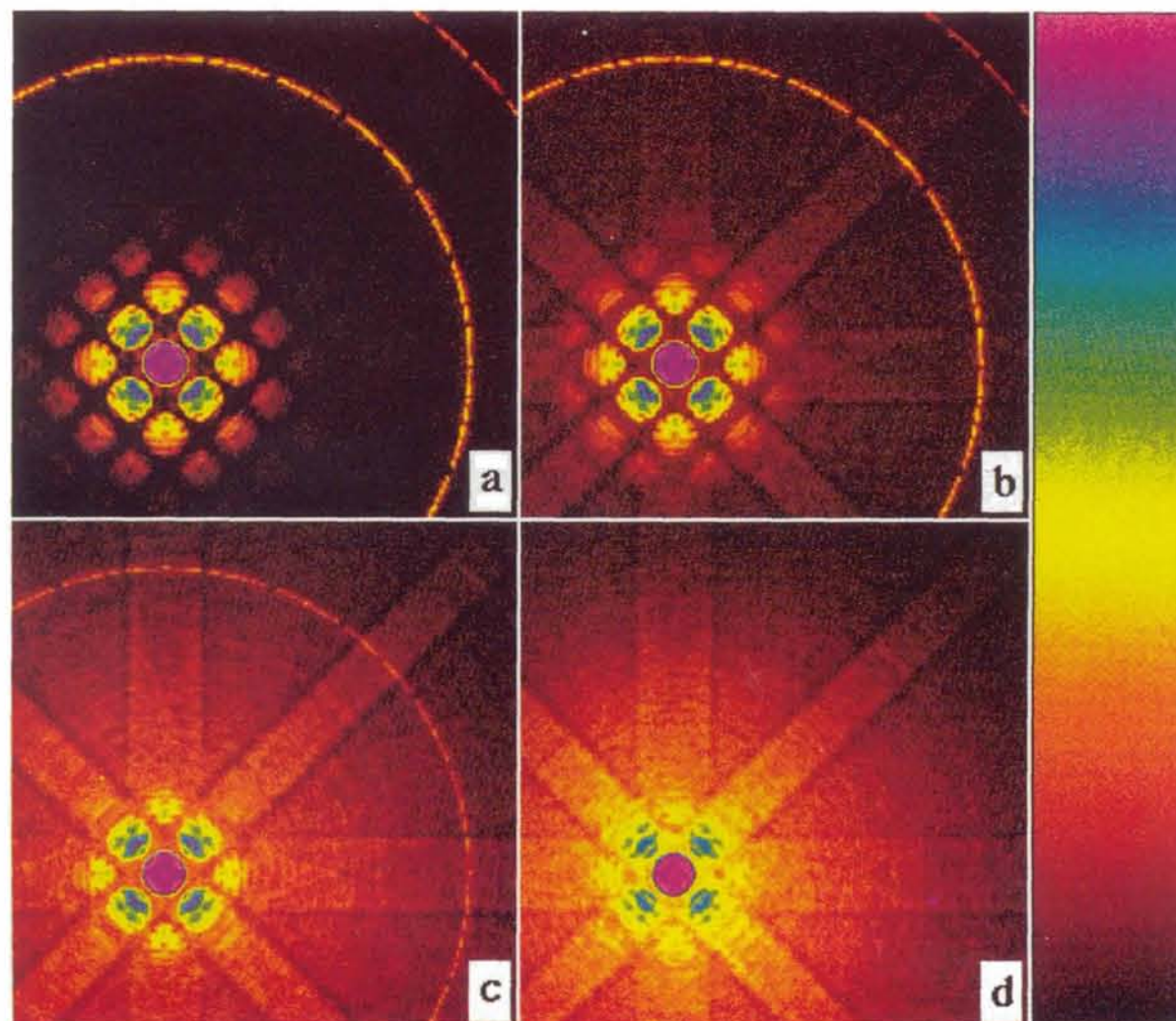
Fig. 3. Vibration series of CBED calculations performed for a 407 Å (300 slices) thick specimen of untilted silicon (100). The r.m.s. vibration amplitudes were (*a*) $0 \cdot 00$, (*b*) $0 \cdot 03$, (*c*) $0 \cdot 07$ and (*d*) $0 \cdot 15$ Å. Each pattern is the ensemble average of 16 phonon configurations. The slice dimensions were 512×512 pixels and 6×6 unit cells, which is $32 \cdot 6 \times 32 \cdot 6$ Å. The incident probe modeled the Cornell VG-HB501 STEM (100 keV) with the low-resolution pole piece ($C_s = 3 \cdot 3$ mm) at Scherzer focus ($\alpha_{ap} = 8 \cdot 18$ mrad, $\Delta f = 1105$ Å).
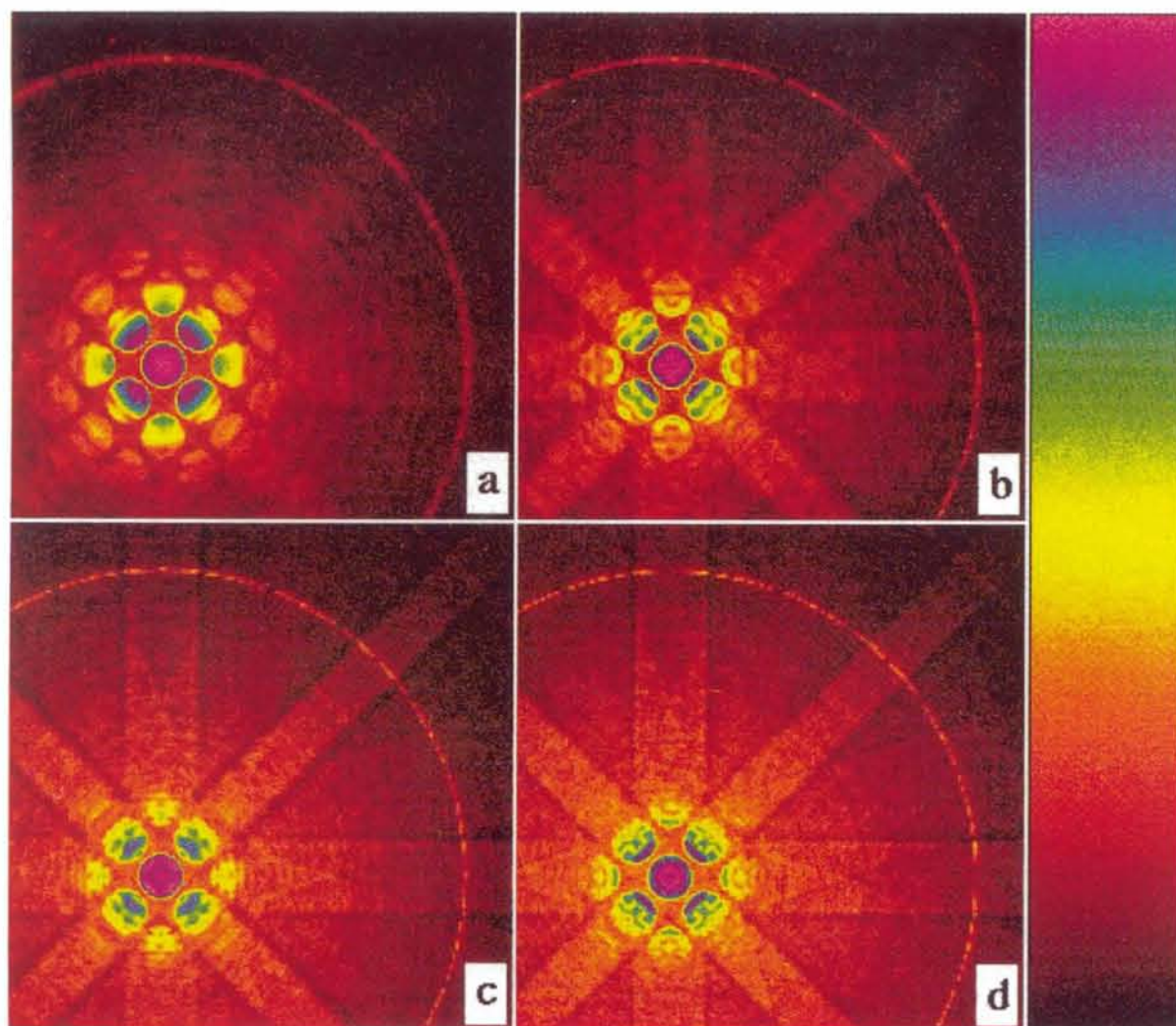
Fig. 5. Thickness series of CBED calculations performed for a specimen of untilted silicon (100). The specimen thicknesses were multiples of 100 slices: (*a*) 136, (*b*) 272, (*c*) 407 and (*d*) 543 Å. The r.m.s. vibration amplitude was 0·07 Å. Each pattern is the ensemble average of 16 phonon configurations. The slice and probe parameters were as for Fig. 3.
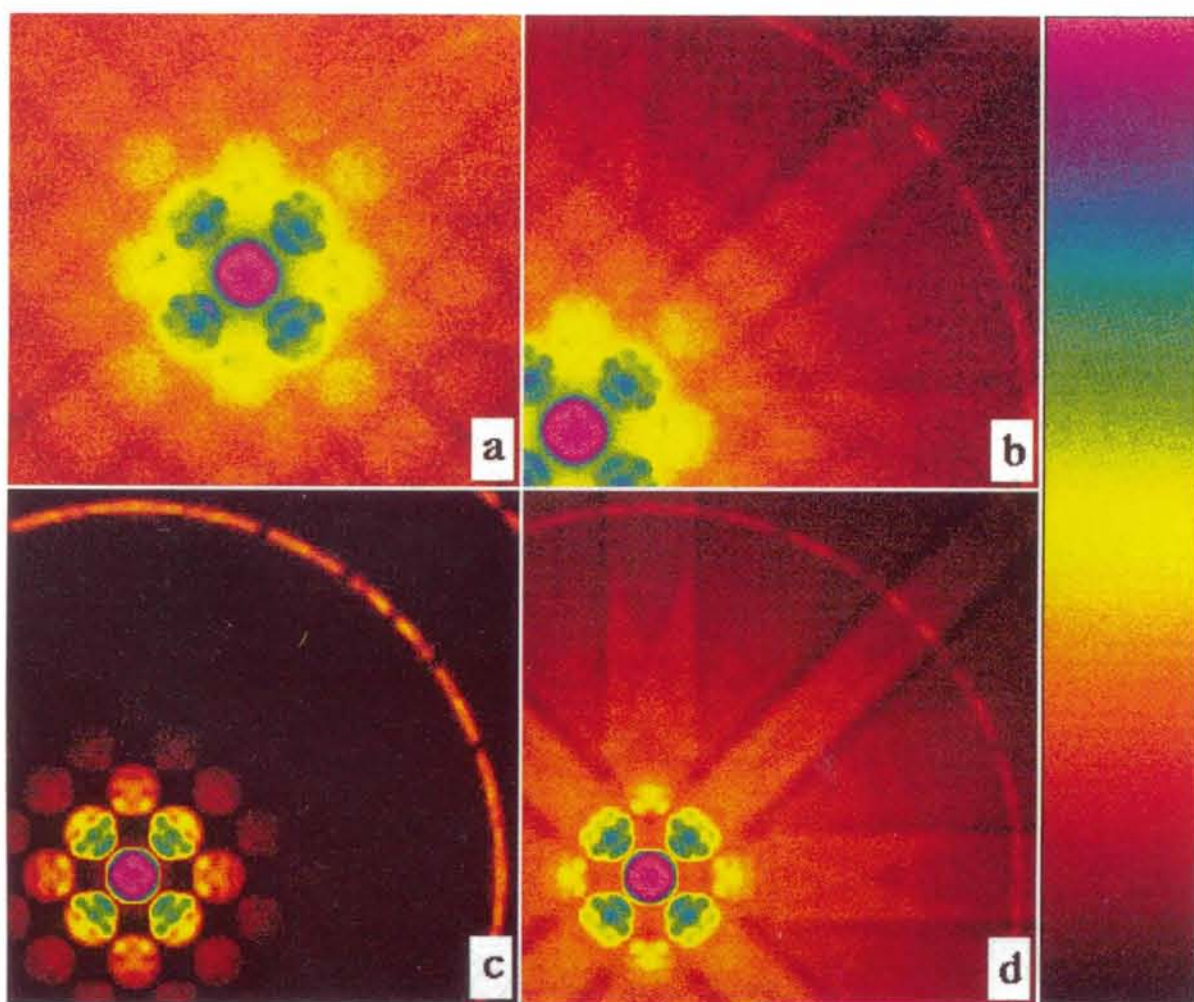

Fig. 8. Comparison of experimental and calculated silicon (100) CBED. Patterns (*a*) and (*b*) are low- and high-angle experimental patterns, (*c*) was calculated with the standard multislice algorithm and (*d*) was calculated with the frozen phonon algorithm. The standard calculation was generated for a 299 Å (220 slices) thick specimen. The frozen phonon calculation is the ensemble average of 64 phonon configurations and was generated for a 326 Å (240 slices) thick specimen and a 0·085 Å r.m.s. vibration amplitude. Both calculated patterns were convolved with a small collector aperture function (1·6 mrad). The incident probe modeled the Cornell VG-HB501 STEM (100 keV) with the low-resolution pole piece ($C_s = 3·3$ mm) near Scherzer focus ($\alpha_{ap} = 7·5$ mrad, $\Delta f = 1100$ Å). The slice parameters were as for Fig. 3.
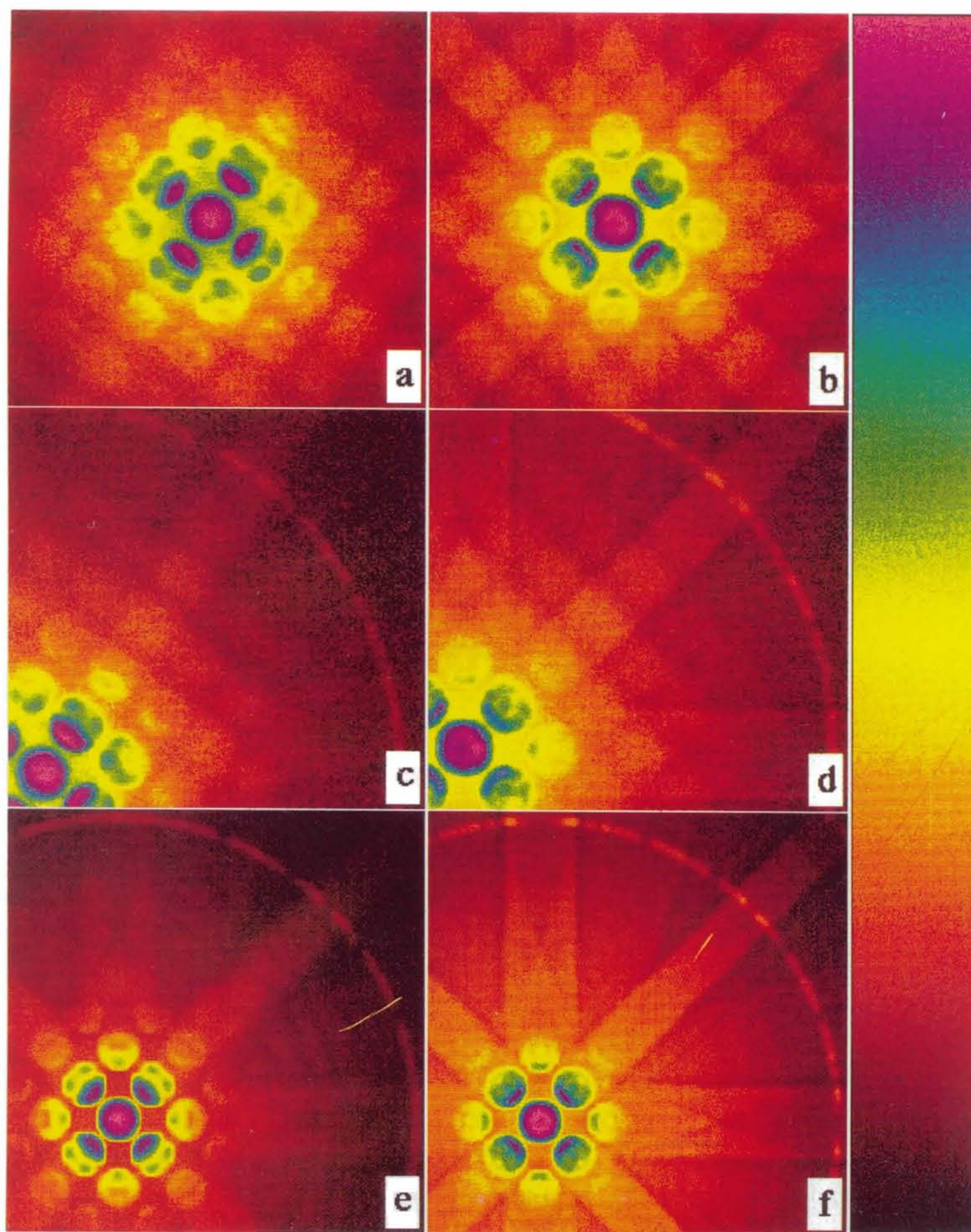
Fig. 10. Additional comparisons of experimental and calculated silicon (100) CBED for different specimen thicknesses. Patterns (*a*), (*c*) and (*e*) form one comparison for an estimated thickness of 217 Å (160 slices) and (*b*), (*d*) and (*f*) form another for a thickness of 543 Å (400 slices). Patterns (*a*) and (*b*) are low-angle experimental patterns, (*c*) and (*d*) are high-angle experimental patterns and (*e*) and (*f*) were calculated with the frozen phonon algorithm. The calculation parameters were as for Fig. 8.

Bragg beam intensity decreases slightly but the weakest beams are lost in the TDS background. The distinctive features in the low-order Bragg-beam discs change slightly with increasing vibration amplitude, consistent with a small lengthening of effective extinction distances. The relatively small change in the low-angle scattering is encouraging since multislice calculations without thermal vibrations have been used to model TEM for many years.

Calculations were performed to explore the effects of varying the specimen thickness. As the specimen thickness is increased, the fraction of intensity in the TDS background rises. Calculated CBED patterns in Fig. 5 show the intensity distribution at a variety of specimen thicknesses. The azimuthal integrations plotted in Fig. 6 provide a more quantitative view of the same data.

Faint Kikuchi bands can be seen in the TDS background, presumably due to phonon scattering coupled with Bragg scattering (Kikuchi, 1928; Kainuma, 1955; Takagi, 1958). This calculation should include multiple Bragg and TDS scattering to all orders. As the atomic vibration amplitude is increased, the bands become more prominent and elaborate, but at large vibrations the fine structure fades away. The Kikuchi bands also become more intense and elaborate with specimen thickness, duplicating structures produced by increased vibration at smaller thicknesses. Therefore, the Kikuchi band structure is an ambiguous measure of the specimen thickness or r.m.s. vibration amplitude.

The intensity in both the TDS background and the HOLZ ring increases with thickness, but their ratio remains roughly constant (Fig. 6). This ratio is very sensitive to the amount of vibration (Fig. 4). The features that depend most strongly on thickness are the peaks and valleys in the low-order Bragg beams (Fig. 5). These features are relatively insensitive to

the amount of vibration (Fig. 3). In a comparison of experimental and calculated CBED patterns, it should be possible to determine the experimental r.m.s. vibration, almost independently of thickness, from the ratio of the TDS to HOLZ intensity. It should also be possible to determine the specimen thickness, almost independently of vibration amplitude, from the low-order Bragg beam features.

One quantitative test of the algorithm and our implementation was to check whether the calculation produced the expected Debye–Waller factors. In the kinematic limit, the Bragg scattering of a monatomic crystal in the presence of thermal vibrations should decrease by a Debye–Waller factor

$$I(\mathbf{k}) = I_0(\mathbf{k}) \exp\left(-4\pi^2 k^2 u_{x\,\mathrm{rms}}^2\right), \qquad (11)$$

where I_0 is the intensity scattered by a perfect (not vibrating) crystal. In frozen phonon calculations, the Debye–Waller factor should arise automatically from the random atomic displacements. The intensity in the HOLZ ring, $k = 3\cdot15\ \text{Å}^{-1} = 117$ mrad, is kinematic scattering for the thicknesses considered here. As a test of the calculation validity, the integrated HOLZ intensity was separated from the TDS background for a variety of vibration amplitudes and specimen thicknesses. As shown in Fig. 7, the HOLZ intensity in the frozen phonon calculations follows the Debye–Waller factor of (11) within an absolute error of 2% for thicknesses up to 543 Å and r.m.s. vibrations up to 0·10 Å. The perfect-crystal intensity, I_0, varies with specimen thickness and was the only free parameter in this fit.

(6) Experimental details

Experimental CBED patterns and electron energy loss spectroscopy (EELS) spectra were taken with a 100 keV VG-HB501 STEM with a low-resolution pole piece ($C_s = 3\cdot3$ mm) near Scherzer focus ($\Delta f = 1100$ Å, $\alpha_{ap} = 7\cdot5$ mrad). Probe widths between 3 and 10 Å were typically achieved. The energy resolution of the EELS spectra was <1 eV.

The CBED patterns were taken by holding the incident beam stationary and scanning the post-specimen electron intensity over a small (1·6 mrad) axial collector aperture. The detector was operated in pulse-counting mode, which has demonstrated single-electron counting, essentially no background, large linear dynamic range and insensitivity to scintillator degradation and afterglow. The detector signal was accumulated into an image by a VAX 3200 workstation (Kirkland, 1990) and stored on disk. This data acquisition technique has the advantage of permitting accurate absolute-intensity measurements over a dynamic range of 10^4, which was essential for a quantitative comparison. The disadvantage is that the field of view is very limited and the signal-to-noise ratio and resolution in the CBED patterns are not ideal.
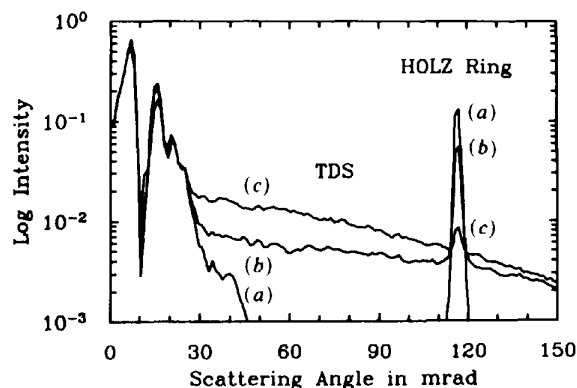

Fig. 4. Logarithm of scattered intensity. The curves were determined by azimuthally integrating the intensities of CBED patterns similar to those shown in Fig. 3, but with different vibration amplitudes. The r.m.s. vibration amplitudes were (a) 0·00, (b) 0·05 and (c) 0·10 Å.

EELS spectra were taken from the same specimen position as some of the CBED patterns. A large (8·8 mrad) collector aperture was used to collect as much plasmon scattering as possible. The detector was again operated in pulse-counting mode and the spectra stored on the computer.

The CBED pattern dimensions were 140× 130 mrad at 256×256 pixels. Since the patterns were recorded serially, each pattern took 2·2 min to record with dwell times of 2 ms pixel^{-1}. Though the Cornell STEM is equipped with an energy spectrometer, it is not possible to take energy-filtered CBED patterns at this time (due to insensitivity in the Grigson coil adjustment). Therefore, there is considerable inelastically scattered intensity, particularly plasmon losses, present in the experimental CBED data. The EELS spectra range was 50 eV at 250 pixels and included the first (16·6 eV) and second (33 eV) silicon plasmon loss peaks. Spectra took 2·1 min to record with dwell times of 500 ms per pixel.
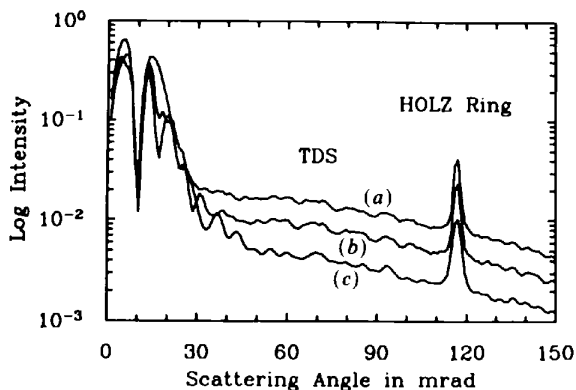

Fig. 6. Logarithm of scattered intensity. The curves were determined by azimuthally integrating the intensities of the CBED patterns shown in Fig. 5. The specimen thicknesses were (a) 136, (b) 272 and (c) 543 Å.
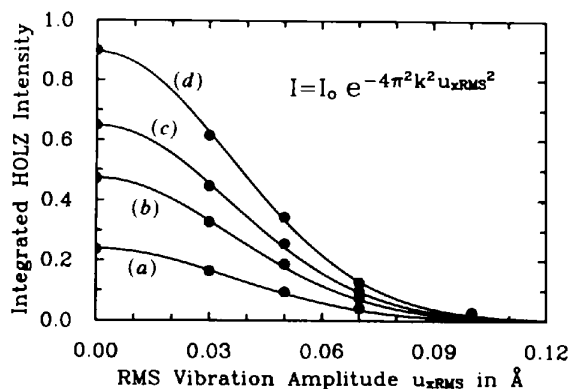

Fig. 7. Integrated HOLZ ring intensities for various specimen thicknesses. The data points were determined by integrating the HOLZ peak intensity, less the TDS background, in the curves shown in Figs. 4 and 6. The specimen thicknesses were (a) 136, (b) 272, (c) 407 and (d) 543 Å.

Specimen drift of up to 10 Å per minute can occur and the beam occasionally drifted to thicker or tilted regions. The action of changing from the small (CBED) to large (EELS) collector aperture shook the microscope slightly and also caused drift. Checks were made to determine whether the specimen had drifted during pattern and spectra acquisition. If so, the data were discarded and the experiment repeated.

Multiple patterns and spectra were taken from the same point to prove that contamination did not seriously degrade the data. In the CBED pattern, contamination slightly increased the low-angle diffuse scattering. In the EELS spectra, contamination produced a small additional plasmon peak at roughly 22 eV. Neither of these effects changed the results of our analysis.

Silicon specimens were thinned by grinding to 20 μm, ion milling until break through and dipping in HF to remove as much of any oxide or amorphous layers as possible. Ion milling was performed at liquid-nitrogen temperatures with 5 kV Ar$^+$ ions and an 18° incidence angle. The specimen was heated under vacuum in the microscope preparation chamber to drive off hydrocarbons and thereby minimize contamination under the beam.

(7) Calculated and experimental CBED comparison

An extension of our previous approach (Kirkland, Loane, Xu & Silcox, 1989) was used to match frozen phonon CBED calculations to experiment. The HOLZ to TDS intensity ratio and the features in the low-order discs were used to make the comparison. The match was performed with 64 configuration calculations at steps in thickness of 27·2 Å (20 slices) and steps in r.m.s. vibration amplitude of 0·01 Å, which set the error in the match to ±14 Å and ±0·005 Å, respectively. The patterns changed significantly with each step. Additional calculations with smaller steps and more phonon configurations should refine the match.

One comparison between experimental silicon (100) CBED patterns, a frozen phonon calculation and a standard multislice calculation is shown in Fig. 8. Note the close match between the frozen phonon calculation and the experiment in the Kikuchi band structure, the HOLZ ring intensity and the features in the low-order Bragg-beam discs. The standard multislice calculation only matches experiment in the low-order Bragg beams.

The finite collector aperture width (1·6 mrad) blurs the features of the experimental CBED patterns. Before comparison to experiment, the calculated patterns were also blurred by a convolution with a top-hat function of the same diameter. The convolution improved the match of the features in the low-order Bragg beams and broadened the HOLZ ring but did not change our estimate of the specimen thickness or

r.m.s. vibration amplitude. Owing to an imbalance in the strength of the Grigson X and Y scan coils, the aspect ratio of experimental CBED patterns was off by up to 8%. The distorted aspect ratio was considered in all the subsequent analyses and has been corrected in the figures.

The best fit for the frozen phonon calculation shown in Fig. 8 occurred with a 0·085 (5) Å r.m.s. atomic displacement and 326 (14) Å thickness. The r.m.s. vibration is larger than the 0·07 Å* expected for room-temperature silicon and corresponds to a temperature of 470 K [by assuming 0·07 Å at 300 K in (4)]. This discrepancy appears too large to be attributed solely to beam heating of the specimen (Reimer, 1984b). It seems more likely that inelastic plasmon scattering, coupled with quasi-elastic and Bragg scattering (Batson & Silcox, 1983), is being included experimentally as additional TDS. An attempt to test this hypothesis with energy-filtered CBED is under way.

The best fit for the standard multislice calculation shown in Fig. 8 occurred with a 299 (14) Å thickness, which is slightly thinner than the best-match frozen-phonon calculation. The difference in thicknesses arises from a reduction in the Bragg scattering in the frozen-phonon calculation, due to the Debye–Waller factor, which increases the extinction distances responsible for the features in the low-order discs. If we apply the Debye–Waller factor of (11) to just the first-order Bragg (220) disc, $k = 0·52$ Å^{-1} = 19·3 mrad, we estimate a lengthening of extinction distances of about 7·5%. Since there is much multiple scattering between low-order Bragg beams, each with its own Debye–Waller factor, this estimate is very crude but it does account for the observed thickness difference.

The match to experiment is not perfect. Fig. 9 shows a quantitative comparison between the azimuthally integrated intensity in the experimental and frozen phonon CBED patterns of Fig. 8. The vertical placement of these curves is arbitrary since the incident-beam current is not known. The match at high scattering angles, >50 mrad, is very good. However, there is more diffuse scattering spreading the intensity in the experimental patterns at low angles than can be accounted for by thermal vibrations. The extra low-angle diffuse scattering can be attributed to scattering by plasmons (Reimer, Fromm & Naundorf, 1990) and possibly a thin oxide or contamination layer on the specimen, neither of which was included in the calculations. The faint broad bands running perpendicular to the Kikuchi bands in the experimental patterns may be the result of correlations between the vibrations of neighboring atoms (Honjo, Kodera & Kitamura, 1964; Komatsu & Teramoto, 1966),

which are neglected in the simple Einstein model used here.

Many additional matches were made at a variety of thicknesses. At no thickness did we notice any significant discrepancy between calculation and experiment other than the excess low-angle diffuse scattering mentioned above. Fig. 10 shows two additional comparisons between experimental CBED patterns and the appropriate frozen phonon calculations for a thinner and a thicker region of the specimen. Fig. 11 shows a more quantitative comparison of the azimuthally integrated intensity in the experimental and frozen phonon patterns in Fig. 10. The excess low-angle diffuse scattering becomes less significant as the thickness is increased, which suggests that an amorphous layer on the specimen surface may be the source. The best fit for the patterns shown in Fig. 10 occurred with exactly the same r.m.s. atomic displacement, 0·085 (5) Å. The best-fit thicknesses were 217 (14) and 543 (14) Å.

(8) Comparison to EELS

Since multiple plasmon scattering follows Poisson statistics (Reimer, 1984a), the ratio of the EELS spectrum intensity in the first plasmon-loss peak to that in the zero-loss peak equals the ratio of the specimen thickness to the plasmon mean free path (MFP). Assuming the specimen thicknesses determined by CBED comparisons (as above) are correct, it is possible to estimate an experimental value for the plasmon MFP from the EELS spectra (Kirkland, Loane, Xu & Silcox, 1989). A comparison of this estimated MFP with other values in the literature provides an independent check of the validity of the frozen-phonon calculation.

EELS spectra were taken with an 8·8 mrad collector aperture from the same positions as some of the
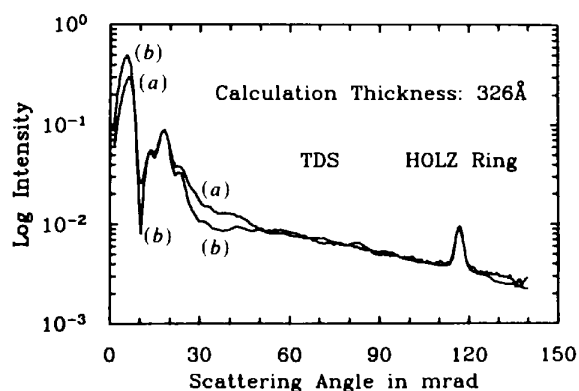
Fig. 9. Comparison of experimental and calculated scattered intensity. The curves were determined by azimuthally integrating the intensities of (a) experimental and (b) frozen phonon CBED patterns in Figs. 8(b) and (d), respectively. The vertical placement of the curves is arbitrary.

---

* See *Note added in proof* on p. 277.

CBED patterns. Plasmon intensities were determined from the spectra by integrating under the zero-loss peak and first plasmon-loss peak at 16·6 eV. The plasmon intensity ratio *versus* the best-match thickness determined from the CBED comparison is plotted in Fig. 12. The slope of the straight-line fit indi-

Fig. 11. Comparison of experimental and calculated scattered intensity. The curves were determined by azimuthally integrating the intensities of (*a*) experimental and (*b*) frozen phonon CBED patterns in Figs. 10(*c*) through (*f*). The vertical placement of the curves is arbitrary.

Fig. 12. Ratio of silicon first-plasmon-loss to zero-loss intensity for a variety of specimen thicknesses. The thicknesses were determined by comparisons of experimental and calculated CBED patterns similar to those shown in Figs. 8 through 11.

cates that the plasmon MFP is 1207 (23) Å. This value agrees well with the experimental value of 1250 Å (8·5 mrad objective aperture, 10 mrad collector aperture) (Sarikaya & Rez, 1982) and the theoretical result of 1150 Å (parallel illumination, 6·5 mrad collector aperture) (Egerton, 1986). These numbers suggest that the frozen phonon calculation determines the correct specimen thickness to within the error of the known value for the silicon plasmon MFP.

The fact that the straight-line fit does not go exactly through the origin is not surprising, considering random error in the data and the possible presence of contamination, oxide or amorphous silicon layers on the specimen (Carpenter & Jang, 1986). The fact that the vertical axis intercept at 10(6) Å is so close to zero is a good indication that the specimen is almost completely crystalline silicon.

Our previous match between silicon (111) CBED and EELS (Kirkland, Loane, Xu & Silcox, 1989) did not include a Debye–Waller factor. At that time we were comparing the experimental CBED patterns to the standard multislice calculation which, as shown above, underestimates the specimen thickness. The net result is a systematic error which overestimates the plasmon MFP. If the previous plasmon MFP result, 1297 (25) Å (8 mrad collector), is reduced by the crude estimate of 7·5% discussed above, the result, 1199 (23) Å, agrees very well with our current work.

The EELS comparison points out that, for all but the thinnest specimens, plasmon scattering is a significant effect. For example, at the 326 Å thickness shown in Fig. 8, 24% of the intensity at small angles has been scattered by plasmons. Since the CBED patterns were not energy filtered, this plasmon scattered intensity makes up a big fraction of the intensity in the experimental CBED patterns above. Even though plasmons scatter predominantly at small angles, coupled plasmon/phonon and plasmon/Bragg scattering can translate inelastically scattered electrons to large angles. To a first approximation, the plasmon scattering at large angles is proportional to the TDS background (Batson & Silcox, 1983). This high-angle inelastic intensity is present in the experimental CBED patterns but is neglected in the calculations. Treating the high-angle inelastic scattering as additional TDS may be the reason that the estimated r.m.s. thermal vibration amplitude is larger than expected.

(9) Discussion

The validity of the frozen phonon technique is strongly supported by a comparison with experimental silicon CBED patterns. This technique naturally produces the Kikuchi band structure, TDS intensity, Debye–Waller factor and lengthened extinction distances, all of which are missing in the standard multislice calculation. The agreement with
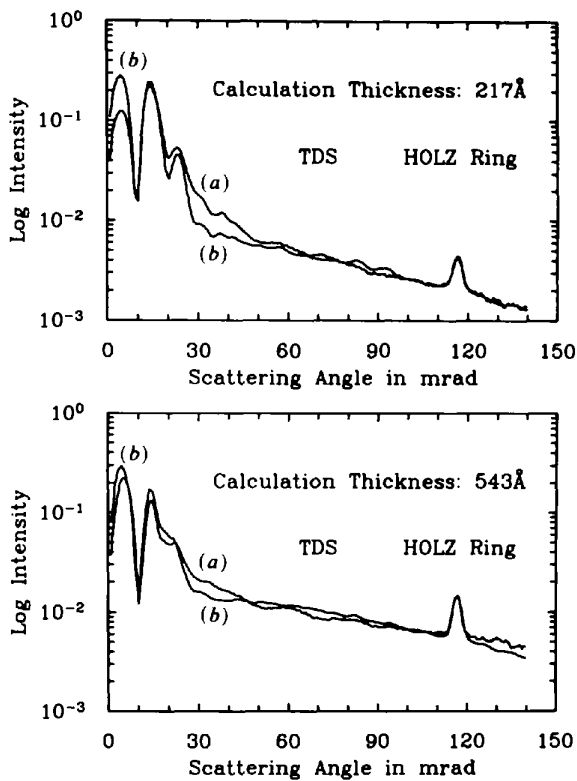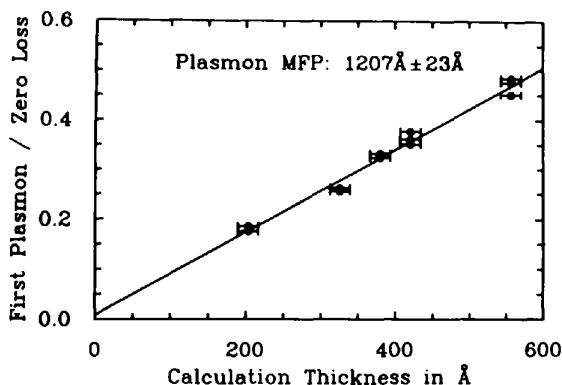
experiment is good for a variety of specimen thicknesses over more than two orders of magnitude of intensity, which is about the precision of the atomic scattering factors. The best-fit r.m.s. vibration amplitude was 0·085 (5) Å for a variety of specimen thicknesses. This value is larger than the 0·07 Å determined at room temperature by X-ray scattering and may represent the inclusion of coupled inelastic/phonon scattering as additional thermal vibration. There is also additional low-angle diffuse scattering in the experimental CBED, which may be the result of plasmon scattering or possibly a thin amorphous layer on the specimen. The silicon plasmon mean free path was estimated from the EELS spectra using the calculation to determine specimen thickness. Comparison with mean-free-path results in the literature indicates that the frozen phonon calculation is accurate to within the error in the known value of the plasmon mean free path.

The frozen phonon calculation is based on a relatively slight modification to the well established multislice algorithm. The Monte Carlo integration closely matches the physical process of electron scattering where millions of single electron diffraction patterns are summed incoherently to produce the average CBED pattern. Multiple thermal diffuse and Bragg scattering to all orders is automatically included in this calculation. Agreement with experiment indicates that appropriate random displacements of the atomic potentials produces a valid representation of the thermal equilibrium potential.

The frozen phonon technique is an alternative route to the prediction of scattered intensities in the presence of thermal vibrations, particularly at large angles. A numerically intensive calculation, based on a simple first-principles model, replaces more-complicated analytical treatments. Thus, this technique provides an independent check of the validity of the elaborate chain of approximations present in more analytical approaches. As computational capabilities continue to increase, the shift from complicated analysis to numerically intensive first-principles models becomes more desirable.

A primary motivation for developing this technique was to provide an improved theoretical basis for the calculation of ADF STEM images. At room temperature, TDS makes up most of the scattering in the range of angles which contribute to the ADF STEM signal. Even at temperatures near absolute zero, there is still significant vibration and TDS from the crystal zero-point energy. The frozen phonon calculation matches experiment very closely in the TDS, which justifies its use in the calculation of ADF STEM images. Since the ADF STEM signal is not usually energy filtered, the use of a larger r.m.s. thermal vibration may be an effective means of including inelastic scattering in ADF STEM calculations. The presence of strong TDS at lower scattering angles

suggests that an inner ADF detector radius as small as 30 mrad may be best. Additional quantitative predictions of the dependence of Z contrast on specimen thickness, defocus, objective aperture choice and detector geometry will be determined.

Note added in proof

Recent experiments and a better background treatment have yielded an improved estimate for the silicon r.m.s. vibration amplitude of 0·080(5) Å. This new estimate agrees with the extremely accurate X-ray measurement of 0·0764(2) Å by Aldred & Hart (1973).

References

ALDRED, P. J. E. & HART, M. (1973). *Proc. R. Soc. London Ser. A*, **332**, 239–254.
BATSON, P. E. & SILCOX, J. (1983). *Phys. Rev. B*, **27**, 5224–5239.
BIRD, D. M., JAMES, R. & PRESTON, A. R. (1987). *Phys. Rev. Lett.* **59**, 1216–1219.
BORN, M. & VON KARMAN, TH. (1913). *Phys. Z.* **14**, 65–71.
CARPENTER, R. W. & JANG, P. R. T. (1986). *44th Annual Proc. Electron Microscopy Society of America*, edited by G. W. BAILEY, pp. 718–719. San Francisco Press.
CARPENTER, R. W. & SPENCE, J. C. H. (1982). *Acta. Cryst.* **A38**, 55–61.
COWLEY, J. M. & MOODIE, A. F. (1957). *Acta. Cryst.* **10**, 609–619.
DEBYE, P. (1914). *Ann. Phys. (Leipzig)*, **43**, 49–95.
DOYLE, P. A. & TURNER, P. S. (1967). *Acta Cryst.* **A24**, 390–397.
EADES, J. A. (1988). *Ultramicroscopy*, **24**, 143–154.
EGERTON, R. F. (1986). *Electron Energy Loss Spectroscopy in the Electron Microscope*, pp. 154–159. New York: Plenum.
EINSTEIN, A. (1907). *Ann. Phys. (Leipzig)*, **22**, 180–190.
FAN, G. Y. (1989). *Ultramicroscopy*, **30**, 359–364.
FUNG, K. K. (1985). *Ultramicroscopy*, **17**, 81–86.
GOODMAN, P. (1975). *Acta Cryst.* **A31**, 804–810.
GOODMAN, P. & MOODIE, A. F. (1974). *Acta Cryst.* **A30**, 280–290.
HALL, C. R. & HIRSCH, P. B. (1965). *Proc. R. Soc. London Ser. A*, **286**, 158–177.
HIRSCH, P., HOWIE, A., NICHOLSON, R. B., PASHLEY, D. W. & WHELAN, M. J. (1977). *Electron Microscopy of Thin Crystals*, pp. 112–116. New York: Kreiger.
HONJO, G., KODERA, S. & KITAMURA, N. (1964). *J. Phys. Soc. Jpn*, **3**, 351–367.
International Tables for X-ray Crystallography (1974a). Vol. III, pp. 233–246. Birmingham: Kynoch Press. (Present distributor Kluwer Academic Publishers, Dordrecht.)
International Tables for X-ray Crystallography (1974b). Vol. IV, pp. 99–101. Birmingham: Kynoch Press. (Present distributor Kluwer Academic Publishers, Dordrecht.)
ISHIZUKA, K. & UYEDA, N. (1977). *Acta Cryst.* **A33**, 740–749.

IUPAC (1990). *Nomenclature of Inorganic Chemistry.* Oxford: Blackwell.

JONES, P. M., RACKHAM, G. M. & STEEDS, J. W. (1977). *Proc. R. Soc. London Ser. A,* **354**, 197-222.

KAINUMA, Y. (1955). *Acta Cryst.* **8**, 247-257.

KELLY, P. M., JOSTSONS, A., BLAKE, R. G. & NAPIER, J. G. (1975). *Phys. Status Solidi A,* **31**, 771-780.

KIKUCHI, S. (1928). *Proc. Jpn Acad. Sci.* **4**, 271-278.

KIRKLAND, E. J. (1990). *Ultramicroscopy,* **32**, 349-364.

KIRKLAND, E. J., LOANE, R. F. & SILCOX, J. (1987). *Ultramicroscopy,* **23**, 77-96.

KIRKLAND, E. J., LOANE, R. F., XU, P. & SILCOX, J. (1989). *Computer Simulation of Electron Microscope Diffraction and Images,* edited by W. KRAKOW & M. O'KEEFE, pp. 13-31. New York: Minerals, Metals and Materials Society.

KOMATSU, K. & TERAMOTO, K. (1966). *J. Phys. Soc. Jpn,* **6**, 1152-1159.

LANGMORE, J. P., WALL, J. & ISAACSON, M. S. (1973). *Optik (Stuttgart),* **38**, 335-350.

LOANE, R. F., KIRKLAND, E. J. & SILCOX, J. (1988). *Acta Cryst.* A44, 912-927.

MARADUDIN, A. A., MONTROLL, E. W., WEISS, G. H. & IPATOVA, I. P. (1971). *Theory of Lattice Dynamics in the Harmonic Approximation,* pp. 304-309. New York: Academic Press.

MITRA, S. S. & MASSA, N. E. (1982). *Handbook on Semiconductors,* Vol. 1, edited by T. S. MOSS & W. PAUL, pp. 81-192. Amsterdam: North Holland.

MOTT, N. F. (1930). *Proc. R. Soc. London. Ser. A,* **127**, 658-665.

PENNYCOOK, S. J. (1989). *Ultramicroscopy,* **30**, 58-69.

PENNYCOOK, S. J. & JESSON, D. E. (1990). *Phys. Rev. Lett.* **64**, 938-941.

PENNYCOOK, S. J., JESSON, D. E. & CHISHOLM, M. F. (1990). *Proc. 6th Conf. on the Microscopy of Semiconducting Materials,* pp. 51-58. Oxford Univ. Press.

PRESS, W. H., FLANNERY, B. P., TEUKOLSKY, S. A. & VETTERLING, W. T. (1986). *Numerical Recipes,* pp. 191-225. Cambridge Univ. Press.

REIF, F. (1965). *Fundamentals of Statistical and Thermal Physics,* pp. 331-346. New York: McGraw-Hill.

REIMER, L. (1984a). *Transmission Electron Microscopy,* pp. 160-166. Berlin: Springer Verlag.

REIMER, L. (1984b). *Transmission Electron Microscopy,* pp. 433-439. Berlin: Springer Verlag.

REIMER, L., FROMM, I. & NAUNDORF, I. (1990). *Ultramicroscopy,* **32**, 80-91.

SAKURAI, J. J. (1985). *Modern Quantum Mechanics,* edited by S. F. TUAN, pp. 89-94, 453. Menlo Park, California: Benjamin/Cummings.

SARIKAYA, M. & REZ, P. (1982). *40th Annual Proc. Electron Microscopy Society of America,* edited by G. W. BAILEY, pp. 486-487. Baton Rouge: Claitors.

SHIN, D. H., KIRKLAND, E. J. & SILCOX, J. (1989). *Appl. Phys. Lett.* **55**, 2456-2458.

SINHA, S. K. (1973). *Crit. Rev. Solid State Sci.* **3**, 273-334.

SPENCE, J. C. H., ZUO, J. M. & LYNCH, J. (1989). *Ultramicroscopy,* **31**, 233-239.

STEEDS, J. W. (1983). *Quantitative Electron Microscopy,* edited by J. N. CHAPMAN & A. J. CRAVEN, pp. 49-96. Glasgow: Scottish Univ. Summer School in Physics.

TAKAGI, S. (1958). *J. Phys. Soc. Jpn,* **13**, 278-296.

TANAKA, M., SAITO, R. & SEKII, H. (1983). *Acta Cryst.* A39, 357-368.

VINCENT, R., BIRD, D. M. & STEEDS, J. W. (1984). *Philos. Mag.* A50, 745-786.

WANG, Z. L. & COWLEY, J. M. (1989). *Ultramicroscopy,* **31**, 437-453.

WILLIS, B. T. M. & PRYOR, A. W. (1975). *Thermal Vibrations in Crystallography,* pp. 34-78. Cambridge Univ. Press.

XU, P., KIRKLAND, E. J., SILCOX, J. & KEYSE, R. (1990). *Ultramicroscopy,* **32**, 93-102.

ZUO, J. M., SPENCE, J. C. H. & O'KEEFFE, M. (1988). *Phys. Rev. Lett.* **61**, 353-356.

ZUO, J. M., SPENCE, J. C. H. & HØIER, R. (1989). *Phys. Rev. Lett.* **62**, 547-550.

On the Application of Phase Relationships to Complex Structures. XXIX. Choosing the Large *E*s

BY G. GERMAIN AND V. NASTOPOULOS*

Unité de Chimie Physique Moléculaire et de Cristallographie, Université de Louvain, 1348 Louvain-la-Neuve, Belgium

AND M. M. WOOLFSON

Department of Physics, University of York, York YO1 5DD, England

Abstract

The set of large *E*s through which a structure is solved by direct methods is usually chosen by a convergence or convergence-divergence process. This process aims to give a strong phase-extension pathway starting from a small set of *E*s whose phases are known or allocated in some way. Sometimes sets of reflexions thus obtained are poorly conditioned and under tangent-formula refinement even initially correct phases will degenerate to randomness. A simple new algorithm has been developed which improves the conditioning of the complete set of reflexions and their relationships and is more appropriate to current trends to start refinement from a complete set of random phases. A particular feature of this algorithm is that it maximizes the minimum number of relationships for any reflexion.

* Now at University of Patras, Patras, Greece.